

Human-like Working Memory from Artificial Intrinsic Plasticity Neurons

Jingli LIU¹, Huannan ZHENG¹, Bohao ZOU¹, Kezhou YANG^{1*}

¹Microelectronics Thrust, The Hong Kong University of Science and Technology (Guangzhou), Guangzhou, 511453, China

E-mail: kezhouyang@hkust-gz.edu.cn

Abstract

Working memory enables the brain to integrate transient information for rapid decision-making. Artificial networks typically replicate this via recurrent or parallel architectures, yet incur high energy costs and noise sensitivity. Here we report IPNet, a hardware-software co-designed neuromorphic architecture realizing human-like working memory via neuronal intrinsic plasticity. Exploiting Joule-heating dynamics of Magnetic Tunnel Junctions (MTJs), IPNet physically emulates biological memory volatility. The memory behavior of the proposed architecture shows similar trends in n -back, free recall and memory interference tasks to that of reported human subjects. Implemented exclusively with MTJ neurons, the architecture with human-like working memory achieves 99.65% accuracy on 11-class DVS gesture datasets and maintains 99.48% on a novel 22-class time-reversed benchmark, outperforming RNN, LSTM, and 2+1D CNN baselines sharing identical backbones. For autonomous driving (DDD-20), IPNet reduces steering prediction error by 14.4% compared to ResNet-LSTM. Architecturally, we identify a 'Memory-at-the-Frontier' effect where performance is maximized at the sensing interface, validating a bio-plausible near-sensor processing paradigm. Crucially, all results rely on raw parameters from fabricated devices without optimization. Hardware-in-the-loop validation confirms the system's physical realizability. Separately, energy analysis reveals a reduction in memory power of $2,874\times$ compared to LSTMs and $90,920\times$ versus parallel 3D-CNNs. This capacitor-free design enables a compact $\sim 1.5\mu\text{m}^2$ footprint (28 nm CMOS): a >20 -fold reduction over standard LIF neurons. Ultimately, we demonstrate that instantiating human-like working memory via intrinsic neuronal plasticity endows neural networks with the dual biological advantages of superior dynamic vision processing and minimal metabolic cost.

Main

Biological intelligence excels at navigating chaotic sensory environments by continuously integrating immediate history to guide decision-making. For example, to safely navigate through traffic, a driver relies not on a single static visual frame, but on the mental retention of vehicle trajectories observed seconds prior—a core cognitive function known as working memory^{1,2}. This biological function allows humans to efficiently track moving objects and predict outcomes in dynamic environments with remarkable precision³⁻⁶. On the contrary, artificial counterparts face a fundamental dilemma. Traditional recurrent architectures, including LSTMs, may struggle to maintain robust representations amidst noisy temporal streams⁷⁻¹¹. Consequently, fields like autonomous driving are pivoted from historical sequence processing towards large-scale parallel inputs typified by Transformer models^{12,13}. While this shift yields superior performance, it comes at a prohibitive cost: energy consumption and hardware overheads that can escalate by orders of magnitude^{14,15}. Ultimately, both established and emerging neural architectures rely on elaborate structural complexity to emulate working memory, failing to achieve the elegant synergy of high efficiency and low metabolic consumption, which can be easily obtained by biological-brains.

In order to obtain brain-level power efficiency with high performance, neuromorphic computing paradigm proposes to construct AI systems by learning from structures and functions of biological brains. By emulating the brain's event-driven signaling, spiking neural networks (SNNs) theoretically promise distinct advantages in power efficiency and latency¹⁶. This paradigm is particularly congruent with dynamic vision sensors (DVS), which capture temporal information as asynchronous, sparse spike streams rather than redundant frames^{17,18}. However, achieving seamless integration of these technologies remains a challenge. Although SNNs are theoretically adept at temporal processing, to ensure competitive accuracy, current models frequently follow complex ANN architecture, such as LSTMs¹⁹ or vision transformers²⁰. Based on this approach, plenty of work proves the effect of power reduction^{20,21}. However, such method favors the compute-dense nature of silicon hardware rather than the efficiency of the biological brain²². Consequently, performance is often constrained by these architectural priors: such models frequently struggle to exceed the accuracy of their ANN counterparts^{23,24}. Furthermore, the reliance on complex, GPU-optimized architectures creates an efficiency bottleneck: although power is reduced, it still remain above the theoretical limits of neuromorphic computing^{25,26}. Fundamentally, addressing these limitations requires looking beyond structural complexity to exploit simple, endogenous biological dynamics. More specifically, for short-term temporal processing, a critical imperative remains: to realize working memory through a native, biologically plausible

mechanism that eliminates complex architectural dependencies, thereby recovering the dual advantages of exceptional energy efficiency and high-performance characteristic of biological intelligence.

To efficiently realize the required bio-plausible mechanisms, neuromorphic computing paradigm proposes the corresponding hardware design²⁷. Emerging microelectronic devices, including resistive RAM (RRAM)²⁸, ferroelectrics²⁹, phase-change memory (PCM)³⁰, spintronics³¹ and others^{32,33}, offer a promising pathway by leveraging device physics to emulate biological behaviors. However, a discrepancy exists between device capability and functional requirements. In particular, realizing higher-order neuronal mechanisms typically demands elaborate circuit designs. For instance, upgrading a standard capacitor-based integrate-and-fire LIF architecture to an adaptive leaky integrate-and-fire (ALIF) configuration necessitates an auxiliary adaptation loop, effectively doubling the circuit footprint^{34,35}. This structural overhead offsets the energy efficiency and scalability gains of neuromorphic systems. To address this, we propose relying on intrinsic device physics to generate complex dynamics, eliminating the need for extensive additional circuitry. Addressing this challenge relies on harnessing intrinsic device physics to generate complex dynamics, avoiding extensive additional circuitry.

In this work, we introduce a hardware-software co-designed neuromorphic architecture that realizes human-like working memory characteristics. Grounded in biologically plausible design, our architecture derives all memory effects solely from neuronal intrinsic plasticity—a biological mechanism enabling short-term memory independent of synaptic connections^{36,37}. We implement the neuronal core using Magnetic Tunnel Junctions (MTJs), exploiting their intrinsic Joule-heating dynamics as the physical source of plasticity without requiring additional control complexity. Evaluation on *n*-back, free recall and memory interference tasks confirms that the system exhibits memory behaviors distinct from traditional recurrent models and distinctively analogous to human working memory. When scaled to complex temporal processing, the architecture (IPNet) achieves 99.65% accuracy on 11-class DVS gesture datasets³⁸ and maintains 99.48% on a 22-class time-reversed benchmark, outperforming recurrent and convolutional baselines sharing identical backbones such as ResNet-LSTM^{39,40} and (2+1)D ResNet⁴¹. Notably, this temporal robustness is exemplified under a challenging generalization regime: when trained on only the initial 20% of event frames, IPNet retains its peak accuracy, whereas the LSTM baseline collapses from 95.31% to 78.30%. Furthermore, in autonomous driving scenarios (DDD-20), IPNet reduces steering prediction error by 14.4%. These results are substantiated by hardware-in-the-loop experiments using raw device parameters, demonstrating power efficiency gains of

2,874 times over LSTMs and 90,920 times compared to parallel 3D-CNNs.

1. Short-Term Intrinsic Plasticity Neuron

Our artificial neuron is built upon a standard magnetic tunnel junction (MTJ) (Fig. 1a), comprising a free magnetic layer and a pinned magnetic layer separated by an oxide tunnel barrier. Free layer magnetization can be manipulated by external stimuli, while pinned layer magnetization remains fixed. The device state is defined by the orientation of magnetization direction of the two magnetic layers. The low (high) resistance parallel (anti-parallel) state refers to the case where the two magnetizations are in the same (opposite) direction. Upon current injection, together with thermal fluctuations, the spin-transfer torque (STT) induces probabilistic magnetization switching of the free layer (Fig. 1b). By incorporating the MTJ into a simple comparator circuit (Fig. 1c), we translate the switching process of the MTJ into corresponding neuronal firing process, where the current pulses at the comparator output become neuron output spikes (Fig. 1d) (see Methods). Crucially, the intrinsic stochasticity of the MTJ renders non-deterministic neuronal firing behavior. In particular, for a given input voltage, the firing probability follows a characteristic sigmoid activation function (Fig. 1e).

During the switching process of STT-MTJ operation, the applied current passes through the device. As a result, Joule heat is an inevitable byproduct. In our proposed neuron model, we harness Joule heat as a mechanism for neuronal intrinsic plasticity. Upon stimulation, device temperature is increased by Joule heat, which enhances the thermal fluctuations. These enhanced thermal fluctuations directly modulate the switching probability of the MTJ⁴². At the neuron functional level, this manifests as a leftward shift in the activation curve, effectively reducing the firing threshold and increasing the firing probability for a certain input. To quantify this effect, we emulated the thermal residue of preceding activity by introducing a pre-heating pulse of varying duration prior to the standard measurement pulse. The resulting measurements exhibit a dynamic form of neuronal intrinsic plasticity: increasing the pre-heating duration triggers a systematic leftward shift in the activation curves (Fig. 1f), which are well-fitted by functions where only the sigmoid mean (x_0 , half of the maximum switching probability) varied. This indicates that the neuron is triggered to more sensitive activated states. Conversely, extending the cooling interval following a fixed pre-heating pulse induces a corresponding rightward shift that eventually restores the neuron to its pristine state from the activated states (Fig. 1g). For instance, the firing probability nearly triples (from 9.5% to 27.4%) immediately after a 500 ns, 0.9 V pre-pulse. This enhancement is transient: introducing a 200 ns cooling interval allows the probability to relax to an intermediate 16.3%. Together, these two dynamics, a rapid, activity-driven sensitization and a passive decay, form the complete physical basis for an intrinsic short-term

memory trace. The neuron innately 'remembers' recent activity via its thermal state and 'forgets' this information over time at zero additional energy cost. This purely physical process thus provides an *in-situ* mechanism for processing temporal information.

Finally, we validated whether this transient thermal plasticity operates effectively under the operational protocols of neuromorphic computing. We drove the neuron with a spiking protocol operating on a 230 ns cycle consisting of a 150 ns SET phase and a 20 ns RESET phase. We utilized the sigmoid mean x_0 as a proxy for the state of neuron, observing that its deviation from the normal state follows an exponential decay (Fig. S1). This exponential decay implies that the current state depends primarily on the input timing of the preceding few cycles. Consistent with this expectation, we found that the state of neuron is strongly modulated by the immediately preceding pulse, while the influence of earlier events decays within just a few operational cycles (Fig. S2). To validate the fidelity of our modeling approach, we benchmarked the software simulations against experimental data, observing a high degree of quantitative agreement (Fig. S3). This confirms that temporal processing occurs *in-situ* and concurrently with spiking activity, eliminating the need for a separate memory management phase. Ultimately, we realize a transient, history-dependent form of intrinsic plasticity without the need for additional components. This design effectively repurposes Joule heating and thermal fluctuations, phenomena conventionally regarded as parasitic, into essential computational resources for processing temporal information.

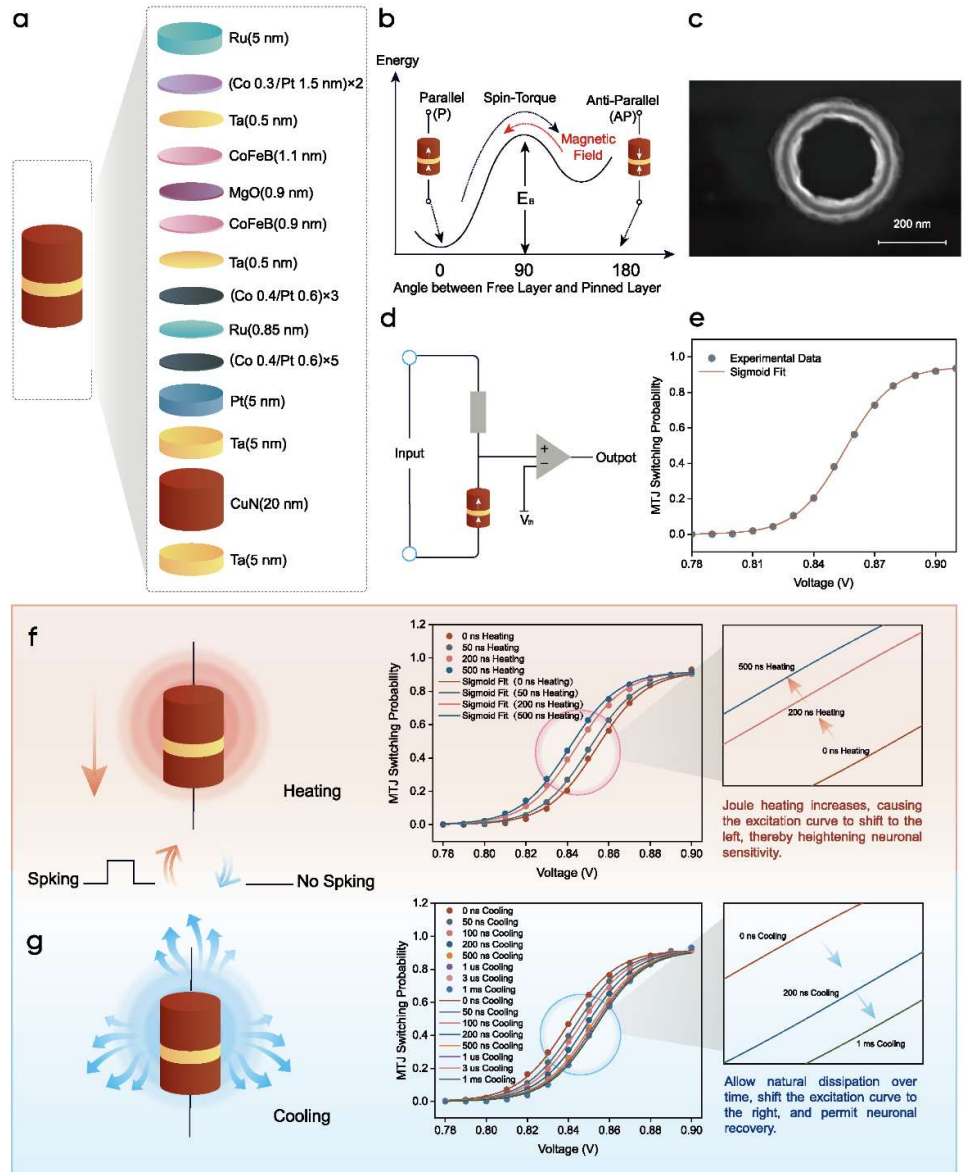


Fig. 1. Device structure and characterization of the MTJ-based stochastic intrinsic plasticity neuron. **a**, Schematic illustration and detailed multilayer stack composition of the MTJ used in this work. **b**, Energy landscape illustrating the switching mechanism between parallel (P) and anti-parallel (AP) states driven by spin-transfer torque (STT). **c**, Top-view SEM image of the fabricated MTJ nanopillar with a diameter of approximately 200 nm. **d**, Simplified circuit schematic of the MTJ-based stochastic neuron. **e**, Switching probability of the MTJ neuron as a function of input voltage, showing experimental data (gray filled circles) and the sigmoid fit (red solid line). **f**, Sensitization of the MTJ neuron induced by Joule heating. The activation curves exhibit a systematic leftward shift as the pre-heating pulse duration increases. **g**, Cooling and recovery dynamics of the MTJ neuron. The activation curves gradually shift back to the

right over time in the absence of input, indicating a return to the initial state. In both **f** and **g**, solid circles represent experimental data, while solid lines denote sigmoid fits obtained by varying only the sigmoid mean (x_0) while keeping other parameters constant.

2. Human-like Working Memory from Neuronal Intrinsic Plasticity

Having established that the thermally plastic neuron exhibits short-term intrinsic plasticity at the single-cell level (Fig. 1), we next investigated the emergent memory characteristics of neural networks composed of these neurons. We introduce the Intrinsic Plasticity Network (IPNet), an architecture where temporal memory arises exclusively from the intrinsic thermal states of its neurons, rather than from recurrent synaptic connections. To isolate the contribution of neuronal dynamics to network performance, we first constructed a minimal version of the network: a simple two-layer fully-connected network (FCN) in which all units, except for the output layer, were our thermally plastic neurons shown in Fig. 1 (see methods in detail). For benchmarking, we also implemented a long short-term memory (LSTM) model of equivalent scale to serve as a baseline for conventional memory architectures.

To characterize the memory dynamics, we employed three cognitive tasks established in human memory research. We found that the IPNet, driven solely by device-based intrinsic plasticity, exhibited short-term memory characteristics strikingly similar to those of humans across distinct dimensions. In contrast, the LSTM demonstrated near-perfect retention capacities on these elementary tasks, a performance profile that diverges significantly from human biological constraints.

We first employed the n -back task⁴³, a widely established measure of working memory (Fig. 2a). In experiments with human subjects, this task requires participants to determine whether a current stimulus matches the n -step earlier stimulus. In our implementation, we presented the network with sequences of simply encoded images (see Methods). As the memory load n increased, the performance of the IPNet, driven by device-based intrinsic plasticity, declined rapidly (Fig. 2b). This trajectory mirrors human performance in similar tasks^{43,44}, suggesting that the IPNet shares a constrained, low-capacity working memory limit, which is typical for biological systems. Crucially, within our architecture, this constraint arises naturally from the heat dissipation of the devices. Consequently, by calibrating device parameters in simulation, we achieved a performance profile that closely tracks human subject data⁴⁴ (Fig. 2b).

Furthermore, to determine whether the IPNet exhibits human-like memory error patterns, we evaluated its susceptibility to proactive and retroactive interference^{45–48}

(extended protocols in Methods). We found that error rates were significantly elevated under interference conditions (Fig. 2e). Notably, this interference effect increased with the similarity between the target and interfering stimuli, echoing the similarity-based interference mechanisms found in biological memory.

Finally, to characterize the temporal dynamics of memory retention, we examined the classic serial position effect⁴⁹ via a free recall task (extended protocols in Methods) (Fig. 2f). The network displayed a robust recency effect, recalling late-sequence items with high probability. Crucially, however, there was a distinctive absence of the primacy effect, which is considered as induced by human long-term memory⁴⁹. That is, the accuracy is not enhanced for initial input items. Instead, recall accuracy for earlier items declined progressively, asymptote to chance levels. Furthermore, introducing a retention interval before retrieval significantly eroded the recency advantage. This time-dependent decay mirrors the transient memory dynamics observed in human subjects performing similar tasks⁴⁹ (Fig. 2f). These findings indicate that the IPNet captures key phenomenological features of biological working memory, specifically its transient nature and capacity constraints.

However, as shown in Fig. 2, the LSTM exhibited near-perfect memory precision across these tasks, significantly diverging from human behavioral patterns. For instance, the LSTM maintained a 100% performance rate (PR) in the n -back task regardless of load n (Fig. 2b), and displayed accuracy invariant to serial position during free recall task (Fig. 2f). This behavior aligns with the conventional view that machine memory far exceeds biological systems in both precision and capacity. Yet, such 'perfect' retention implies the storage of substantial redundant information. Given that the human brain functions efficiently with limited working memory, we raise a critical question: is this information redundancy a key factor preventing artificial neural networks from achieving bio-plausible energy efficiency and competence in complex, inherently noisy real-world scenarios?

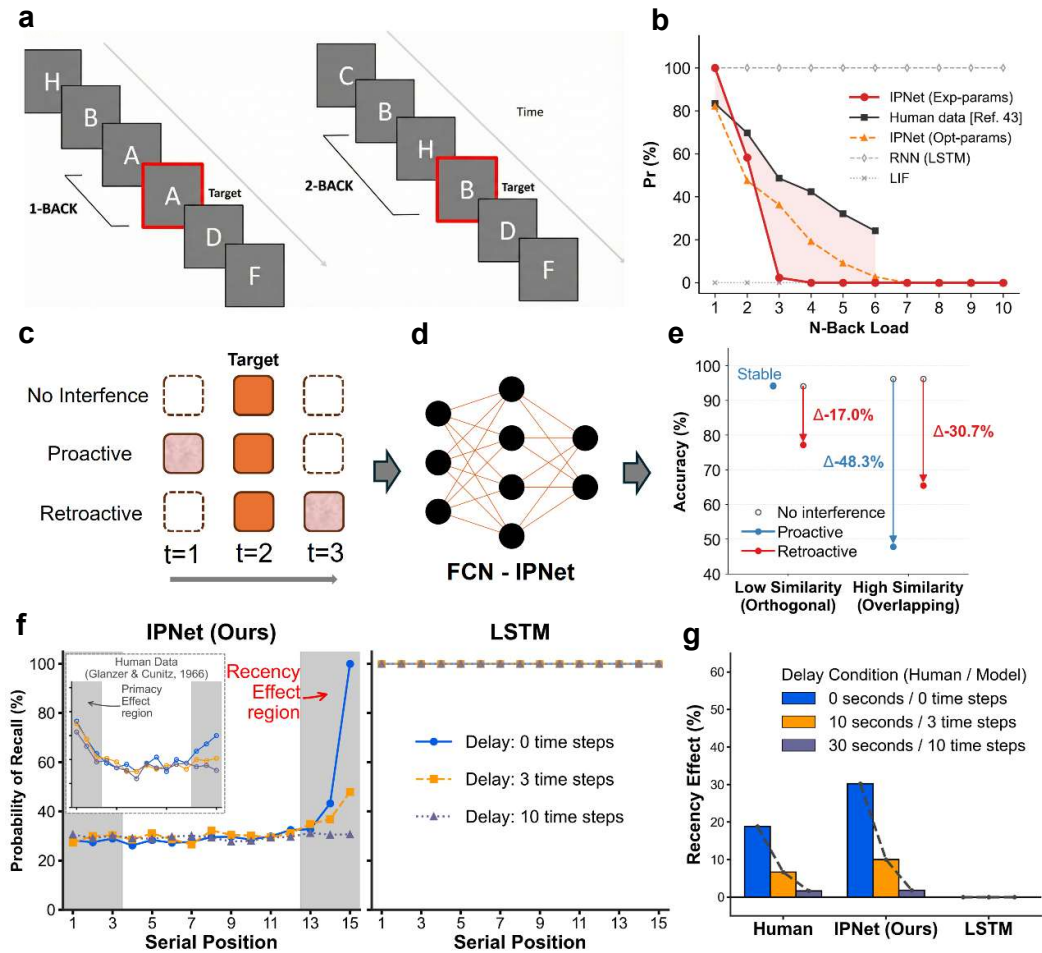


Fig. 2. Emergence of human-like working memory characteristics enabled by neuronal intrinsic plasticity. **a**, Schematic illustration of the n-back task, using 1-back and 2-back conditions as examples. Participants are required to determine whether the current stimulus matches the one presented n steps earlier. **b**, Performance comparison in the n -back task between models and human data [Ref. 43]. **c**, Experimental protocol for memory interference. Trials consist of three-time steps ($t=1, 2, 3$) involving target items (dark squares), distractor items (light squares), or no input (dashed squares). Proactive interference: a distractor precedes the target ($t=1$). Retroactive interference: a distractor follows the target ($t=3$). Control: no distractors are present. **d**, Simplified topology of the FCN-IPNet. **e**, Relative accuracy degradation of the FCN-IPNet under proactive and retroactive interference compared to the control group, tested with low (orthogonal) and high (overlapping) similarity between target and distractor. **f**, Serial position curves in a free recall task for IPNet and LSTM compared with human data in Ref. 49. Blue, yellow, and gray lines represent recall accuracy after retention intervals of 0-, 3-, and 10-time steps (corresponding to 0 s, 10 s, and 30 s for humans), respectively. Note that LSTM traces overlap at the top due to perfect retention (100%

accuracy) across all conditions. **g**, Decay of the recency effect over time. The recency effect (%) is calculated as the difference between the average accuracy of the last 3 serial positions (recency region) and the middle 5 positions (to minimize the influence of primacy and recency effects).

3. Dynamic Vision Enhancement by Human-like Working Memory

Distinct from the conventional LSTM architecture, our IPNet exhibits human-like behavioral constraints across memory tasks. Having established this biological fidelity at the network level (Sec. 2), we next investigated whether these apparent limitations, namely, restricted capacity and temporal imprecision could paradoxically confer an advantage in dynamic visual processing, since the proposed IPNet may not be affected by unnecessary redundant information, similar to human behavior^{3,50}. To validate the existence of such advantage, we constructed IPNet-18 on an adapted common ResNet-18⁵¹ backbone, creating an all-MTJ SNN (see Methods). This network has simple 2D feed-forward architecture, deliberately avoiding recurrent synapses and multi-frame parallel inputs commonly used for temporal processing in dynamic vision. Instead, all temporal information is processed solely by the intrinsic, physical memory of its thermally-plastic MTJ neurons.

We first evaluated the model on the standard 11-class DVS Gesture dataset, which consisted of event streams from subjects performing distinct hand gestures (Fig. 3a). In this task, IPNet-18 achieved an accuracy of 99.65%, outperforming both the spatial baseline (ResNet-18: 97.22%) and temporal variants (LSTM: 97.22%, R(2+1)D-18: 97.92%) (Fig. 3b). Additionally, replacing the intrinsic plasticity neurons in IPNet18 with LIF neurons achieved an accuracy of 97.57%. Notably, this result of IPNet-18 was achieved using parameters directly obtained from experimental measurement of the fabricated MTJs, without software-level data augmentation. Despite this constraint, IPNet-18 still surpasses other reported software results (Fig. S4).

However, this result masked a critical confound: the purely spatial ResNet-18 baseline, devoid of any temporal processing modules, still achieved a high accuracy. Furthermore, architectures with distinct temporal capabilities, RNN and LSTM, yielded identical results (97.22%). These results confirm that the standard DVS Gesture task is insufficient for rigorously distinguishing temporal processing abilities, as spatial information contained in DVS Gesture dataset dominates the classification.

To emphasize the temporal processing capabilities, we introduced a more demanding ‘Time-Reversed DVS Gesture task’, where the chronological order of the event stream is strictly inverted while spatial coordinates are preserved. This task requires the network to distinguish between a gesture and its time-reversed version (22 classes in total), based solely on temporal sequence. The spatial-only baseline collapsed to half of the original accuracy (ResNet-18: 48.61% from the previous 97.22%), indicating that the model has completely no capability to distinguish the same gesture in different

temporal orders. Crucially, we compared IPNet against three prevailing temporal paradigms: (1) Recurrent Architectures (LSTM/RNN), which rely on cyclic connections; (2) Spatiotemporal Convolutions ((2+1)D ResNet), and (3) Vision Transformers (ViT), which employ global self-attention. All the three types of models (LIF: 84.38%; RNN: 93.92% from 97.22%; LSTM: 95.31% from 97.22%; (2+1)D-ResNet18: 96.88% from 97.92%) showed a performance drop from the original task. Conversely, the Vision Transformer (ViT) proved susceptible to overfitting in DVS Gesture task. Even with architectural scaling, accuracy plateaued at $\sim 70\%$. In contrast, IPNet-18 (which same as the last task) maintained 99.31% accuracy (previously 99.65%) (Fig. 3b), decisively outperforming all other models.

Crucially, by harnessing the intrinsic physical dynamics of the device for memory, IPNet achieves temporal processing capabilities with negligible parameter and energy overhead. This stands in sharp contrast to conventional architectures (such as LSTM and R(2+1)D), which demand millions of additional parameters and extensive computational operations to capture temporal information (Fig. 3e). Specifically, regarding the memory and temporal processing for each DVS Gesture sample, IPNet18 consumes merely ~ 87 uJ. To insure a rigorous comparison, we isolated the energy costs strictly attributed to temporal processing for the baselines by subtracting the consumption of a standard spatial-only ResNet18 from the ResNet18-RNN, ResNet18-LSTM, and (2+1)D ResNet18 models (see Methods). Even when deployed on GPUs with advanced process nodes, these isolated temporal components incur substantial energy overheads of 0.21 J, 0.25 J, and 7.91 J, respectively. Consequently, IPNet18 delivers a remarkable energy efficiency improvement of approximately 2,414 times, 2,874 times, and 90,920 times. This suggests that physical neuronal dynamics offer a more efficient substrate for temporal processing than allocated architectural complexity.

The power of this human-like working memory paradigm was further evidenced by its temporal robust generalization. When trained with the first 20% frames in each sample of the original dataset, RNN, LSTM, and (2+1)D ResNet achieve accuracies of 96.18%, 96.18%, and 96.88%, respectively. However, performance on the reversed dataset reveals critical limitations. RNN and LSTM suffer significant drops to 68.92% and 78.30%, indicating that the reduction in frame count severely impacts their temporal processing. While (2+1)D ResNet appears robust (96.53%), this performance is heavily contingent on a sliding window strategy; without it, its accuracy deteriorates to 90.28% and 89.41% on the original and reversed partial datasets, respectively. This indicates that the reduction in frame count significantly impacted their temporal processing (Fig. 3e). On the contrary, our IPNet maintains high accuracy at 99.48% (99.31% when trained with all frames). This contrast highlights IPNet's outstanding capability in generalizing temporal features.

We further investigated how performance is affected by the position of this physical memory in the network. An architectural ablation revealed a what we call 'Memory-at-the-Frontier' effect: performance was maximized when memory was placed at the input

layer (99.31%), substantially decreased after the first convolutional layer (95.66%), and collapsed right before output layer ($\sim 50\%$) (Fig. 3d).

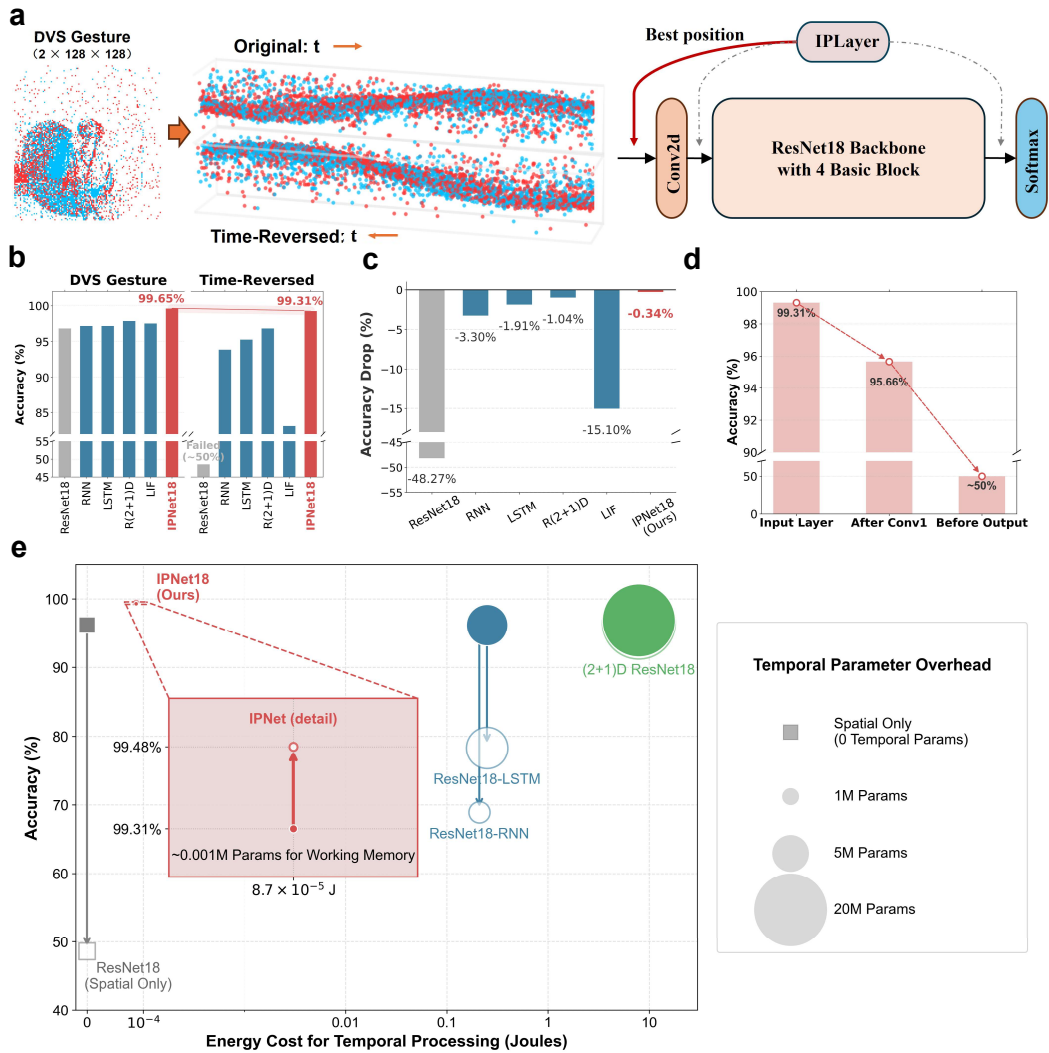


Fig. 3. High-performance and energy-efficient dynamic vision enabled by human-like working memory. **a**, Schematic illustration of the IPNet18 framework processing the DVS Gesture dataset and its time-reversed variant. The time-reversed data retains identical spatial features to the original stream but follows a strictly inverted temporal sequence. **b**, Performance comparison between IPNet18 and other models on both the original and time-reversed DVS Gesture datasets. **c**, Accuracy degradation observed across different models when transitioning from the original to the time-reversed task, highlighting the temporal robustness of the IPNet18. **d**, Accuracy degradation on the Time-Reversed DVS Gesture task as the position of the memory-endowing IPLayer shifts to deeper layers. **e**, Performance versus energy efficiency landscape. Solid markers represent accuracy on the full sequence (circles for the Time-Reversed task, squares for the Original DVS Gesture), while open markers denote performance on the

Time-Reversed task using only the first 20% of frames. The horizontal axis displays the incremental energy cost required for temporal processing relative to the ResNet18 baseline, with bubble size proportional to the incremental parameter overhead (parameter increase relative to the spatial-only backbone). Notably, the IPNet achieves superior performance and robustness with negligible energy and parameter costs.

4. End-to-End Driving

While the forementioned human action tasks demonstrated IPNet's ability to disentangle temporal sequences in structured environments, a critical question remains: can this intrinsic physical memory scale to the continuous, high-entropy domain of real-world control systems? Unlike classification tasks where targets are discrete, autonomous driving requires the continuous regression of steering angles under the stochastic noise of variable lighting, weather, and road environments.

To validate the robustness of our human-like working memory in this complex environment, we evaluated the model on the DAVIS Driving Dataset 2020 (DDD20)⁵² (Fig. 4a). This dataset, currently the largest real-world driving dataset for neuromorphic vision sensors, comprises over 51 hours of data recorded across 4,000 km of diverse highway and urban scenarios. We followed the training and testing set generation procedures from Ref. 53, exclusively utilizing the DVS data. The network processed sequential driving frames, enabling the memory module to capture historical information and predict the instantaneous or future steering angle.

We compared our approach with the standalone ResNet-18, which serves as a memoryless baseline. In this complex application, the behavior of the memory module is consistent with our findings in action recognition: human-like memory, despite its limited capacity and intrinsic noise, outperformed the 'dissipationless' memory typical of conventional ANNs. We employed Root Mean Square Error (RMSE) and Explained Variance (EVA) to quantify performance^{52,53}. Across two lighting conditions (day and night), IPNet-18 achieved a 10-30% reduction in prediction error (RMSE versus human ground truth) compared to the standalone ResNet-18 (Fig. 4b). The EVA results also outperformed ResNet-18 under both lighting conditions (Fig. 4b).

We also tested the CNN-LSTM architecture^{39,54}, which is commonly utilized in end-to-end autonomous driving⁵⁵. However, the inclusion of the LSTM yielded negligible performance gains over the memoryless baseline. Such negligible performance enhancement is also observed in other autonomous driving datasets and tasks by different memory models^{11,56}. This phenomenon stands in contrast to the inherent reliance of human drivers on historical context⁵⁷. It suggests that compared to the

comprehensive, complex history retained by traditional LSTMs, the historical information extracted by the limited-capacity, human-like working memory can be more effectively utilized by the neural network, thereby facilitating decision-making strategies that resemble the history-dependent nature of human driving.

Finally, we also observed the 'Memory-at-the-Frontier' effect in the steering angle prediction tasks in DDD20 dataset. As shown in Fig. 4c, the best performance is obtained when IPLayer is positioned at the input. In contrast to traditional RNN-based architectures, where memory modules are typically integrated after convolutional feature extraction, we found that positioning our module at the input layer (a 'near-sensor' configuration) yielded optimal performance across diverse tasks and architectures. Moreover, the performance progressively declined as the module was positioned deeper within the network. Specifically, in the DDD20 steering prediction task, placing our module after convolutional feature extraction or an additional fully connected layer both resulted in performance degradation. This trend is consistent across completely different tasks (autonomous driving (Fig. 4c), action recognition (Fig. 3d) and n -back (Fig. S5)) and architectures (CNN and FCN).

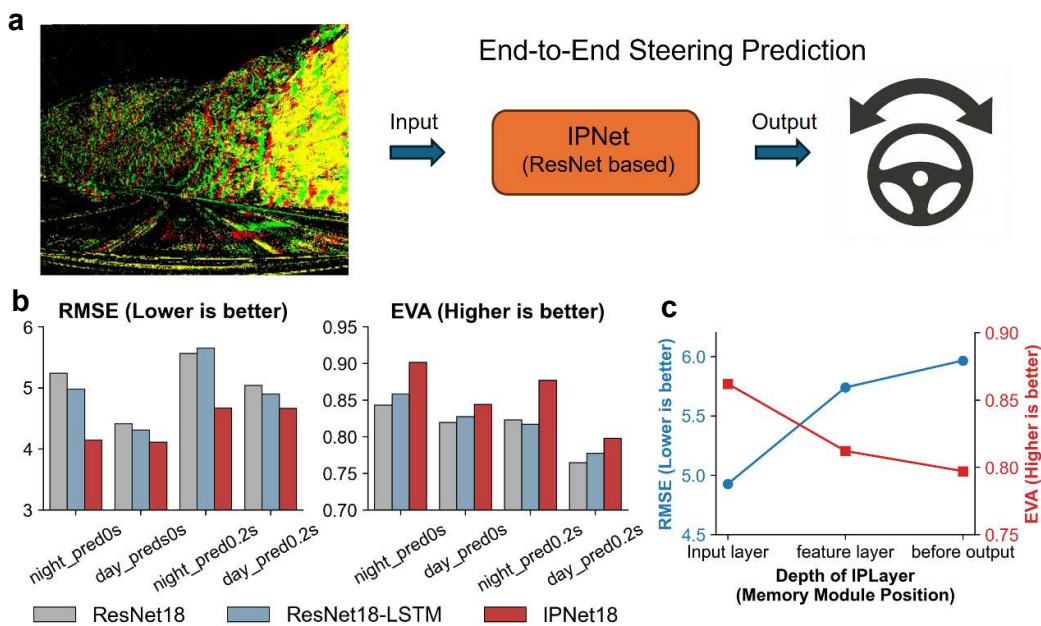


Fig. 4. Real-world application for working memory: End-to-end steering prediction on the DDD20 dataset. **a**, Schematic illustration of the end-to-end steering angle prediction framework. **b**, Performance evaluation under varying environmental conditions (day versus night) and prediction horizons (instantaneous steering angle versus 0.2 s look-ahead). The IPNet18 (red bars) is benchmarked against baselines using Root Mean Square Error (RMSE, lower is better) and Explained Variance Accuracy (EVA, higher is better). **c**, Impact of the memory module's depth on

regression performance. RMSE (blue, left axis) and EVA (red, right axis) are plotted as a function of the IPLayer's position, illustrating the sensitivity of the task to the placement of temporal processing units.

5. Hardware-in-the-Loop

To validate the physical feasibility and advantages of our device-based human-like working memory, we implemented a hardware-in-the-loop system using MTJ devices as a memory module within a neural network. The system operated on a 230-ns cycle and utilized 8 MTJ devices: seven with larger diameters (150-200 nm) that exhibited significant thermal effects, and one smaller device (100 nm) with negligible thermal effects serving as a reference for differential neurons (see Methods). Given constraints on device availability, the device IP-module was positioned after the feature extraction stage, which followed the IPNet-18 architecture described in Sec. 3. The whole IPLayer was formed by 49 device neurons, achieved by reusing the thermal and reference MTJs.

We evaluated the system with device IP-module on an end-to-end steering angle prediction task using the DDD20 dataset. The model was trained in software using device parameters extracted from prior experiments. During inference, the core memory layer of the IPNet was executed entirely in hardware, while the remaining layers were computed in software (Fig. 5a). To extract the temporal information, both the thermal and reference MTJs received identical temporal inputs (see Methods). In this way, consistent with the mechanism demonstrated in Sec. 1, the network's memory capacity was derived exclusively from the residual Joule heat retained by the devices from operations in previous frames.

Fig. 5c presents the inference results for a 600 frames driving sequence from the test set. The experimental hardware results closely tracked the software simulations, with RMSE increasing slightly from 4.020 to 4.198 and EVA decreasing from 0.953 to 0.948. Crucially, the system significantly outperformed the software simulation where device memory effects were absent, which proved that the real devices possess prominent human-like working memory effect we leveraged in our IPNet. For comparison, we trained an LSTM model of equivalent size, consisting of a ResNet-18 backbone and a 49-neuron LSTM layer. Despite operated with coarse device parameters and an unoptimized experimental workflow, our hardware-implemented IPNet consistently outperformed the full-precision software LSTM (RMSE: 5.77, EVA: 0.939) across the tested sequences.

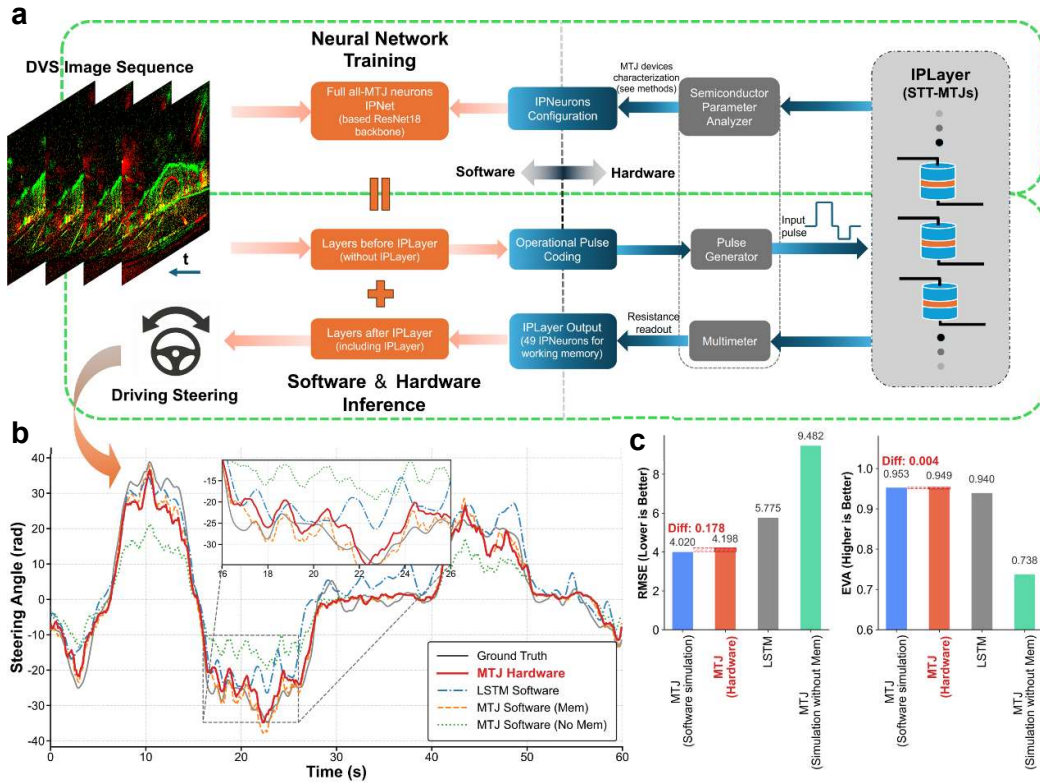


Fig. 5. Hardware-in-the-loop validation of MTJ-based intrinsic plasticity-enabled working memory. **a**, Schematic illustration of the hardware-in-the-loop (HIL) experimental framework applied to the DDD20 end-to-end steering prediction task. **b**, Representative steering angle trajectories over a continuous 60-second (600-frame) test sequence. **c**, Quantitative performance characterization of the hardware implementation, software simulation, and LSTM baseline over the 600-frame test sequence shown in **b**. The results demonstrate a high degree of consistency between the physical MTJ hardware and software models (with marginal deviations of 0.178 in RMSE and 0.004 in EVA), confirming the reliability of the simulation. Furthermore, the MTJ-based hardware system outperforms the full-precision software LSTM, validating the physical realization of efficient, human-like working memory advantages.

Discussion

The capacity to extract coherent feature from chaotic sensory fluxes is a hallmark of biological intelligence, underpinned by the temporal integration mechanisms of working memory². While conventional recurrent architectures (e.g., LSTMs) strive for ‘perfect’ retention over working memory timescales, our IPNet adopts a distinct approach grounded in biological constraints. Validated through n-back, free recall, and interference tasks, our system exhibits the hallmark traits of previously reported human subjects: limited capacity and transient decay. We posit that this “imperfection” is, in

fact, an evolutionary asset: biological systems likely leverage rapid decay to filter stochastic noise from dynamic environments, thereby focusing attention on the immediately relevant temporal window. Our comparative analysis supports this view. On a challenging time-reversed gesture benchmark designed to probe temporal processing capability, architectures engineered for extensive retention, ResNet-LSTM and (2+1)D ResNet, plateaued at 95.31% and 96.88% accuracy, respectively. In contrast, by leveraging human-like working memory characteristics, IPNet achieved a superior accuracy of 99.48%. This indicates that excessive historical context can hinder dynamic interpretation. This advantage extends to real-world scenarios, where IPNet reduces steering prediction error (RMSE) by 14.4% compared to ResNet-LSTM baselines. These findings suggest a divergence in optimal memory mechanism based on task modality: while symbolic tasks (e.g., NLP) demand the precise context of Large Language Models^{58,59}, dynamic vision relies on the dissipative properties inherent to biological systems—highlighting that biological "forgetting" is not a flaw, but an adaptation for processing continuous, high-entropy sensory streams.

Furthermore, we demonstrate that such human-like working memory can emerge solely from neuronal intrinsic plasticity, independent of the complex recurrent synaptic connections typically required in ANNs. By leveraging the neuron's inherent capability to maintain short-term memory traces via its physical state, this approach eliminates the need for elaborate architectural overhead. Consequently, we achieve optimization via hardware-software co-design: utilizing device underlying physics to emulate neuronal intrinsic plasticity, the effective working memory can be efficiently realized, which leads to high-performance-low-consumption characteristics similar to biological agents. Moreover, our architecture aligns with the emerging "activity-silent" working memory framework in neuroscience⁶⁰⁻⁶², showing the computational efficacy of retaining information through the transient dynamics of intrinsic neuronal states without relying on persistent spiking activity. On the other hand, while most recent progress was made in the aspect of power reduction, utilizing the spike sparsity or synaptic in-memory computing^{21,33}, our results indicate that physically emulating distinct biological mechanisms can represent a practical way of performance improvement.

Architecturally, we observed that the intrinsic plasticity module maximizes performance when positioned at the input layer. We term this phenomenon the 'Memory-at-the-Frontier' effect, a consistent finding across distinct architectures and disparate tasks, including the n -back task (Fig. S5), Time-Reversed DVS Gesture recognition, and end-to-end steering angle prediction. This configuration mirrors biological organization, where retinal and cochlear systems perform immediate

temporal adaptation. This discovery offers a theoretical foundation for the emerging paradigm of near-sensor computing⁶³. Near-sensor computing is not merely an energy-saving strategy for reducing data transmission, but a computational imperative: temporal correlations in raw sensory data are most effectively extracted at the sensing end before spatial abstraction occurs. This principle validates a hierarchical design where physical dynamics handle immediate sensory buffering, unburdening downstream digital logic for higher-level reasoning.

Crucially, the utility of this intrinsic memory mechanism is not limited to specific network topologies. We demonstrated its effectiveness on representative backbones, specifically FCN and ResNet, spanning both SNN and ANN coding schemes. This universality reinforces the conclusion that "neuromorphic" qualities can be imbued into standard ANNs by integrating biologically plausible mechanisms, independent of the signaling format (spikes vs. continuous values). By effectively turning any standard neural unit into the proposed history-dependent counterpart, our approach offers a flexible, plug-and-play solution that bridges the gap between biological dynamics and mainstream deep learning architectures, with significant room for further optimization in network configuration.

Finally, the physical realization of this architecture underscores the potential of harnessing thermodynamic entropy as a computational resource. We repurposed Joule heating, conventionally a parasitic effect to be suppressed, as a functional computational resource. This *in-situ* calculation enables the realization of working memory with zero additional circuit footprint, achieving a neuron size of $\sim 1.5 \text{ um}^2$ (including CMOS circuitry) and a core device area of merely 0.03 um^2 . Meanwhile, such *in-situ* calculation also underpins the observed orders-of-magnitude gains in power efficiency ($2,874\times$ reduction compared to LSTMs and $90,920\times$ compared to parallel 3D-CNNs). Moreover, the underlying principle is device-agnostics: the mechanism relies on the generic physics of relaxation effect rather than the specific properties of MTJs. Consequently, this framework is robust to parameter variations and can be generalized to a broad class of dissipative devices (e.g., phase-change or resistive memories), offering a versatile hardware substrate for the next generation of energy-efficient, biologically inspired edge intelligence.

Methods

MTJ fabrication

The MTJ devices are fabricated with a stack structure as follows, from the substrate side: Ta(5)/CuN(20)/Ta(5)/Pt(5)/[Co(0.4)/Pt(0.6)]₅/Ru(0.85)/[Co(0.4)/Pt(0.6)]₃/Ta(0.5)/Co₂₀Fe₆₀B₂₀(0.9)/MgO(0.9)/Co₂₀Fe₆₀B₂₀(1.1)/Ta(0.5)/[Co(0.3)/Pt(1.5)]₂/Ru(5) (Fig. 1a). The numbers in parentheses indicate the layer thickness in nanometers. The films were patterned into nanopillars using a standard nanofabrication process. First, the bottom electrodes were defined by ultraviolet (UV) photolithography and ion beam etching. Next, the MTJ pillars were patterned using electron-beam lithography (EBL) and etching. An insulating SiO₂ layer was then deposited, followed by a lift-off process to expose the pillar tops. Finally, the top contact pads were fabricated using UV photolithography followed by metal deposition and a lift-off process.

Device thermal effects characterization

All electrical measurements were performed using a Keithley 4200A-SCS semiconductor parameter analyzer equipped with a 4225-PMU pulse measure unit and a 4225-RPM remote amplifier/switch. All measurements were performed at room temperature and atmospheric pressure in the absence of an external magnetic field. The switching probability P_{sw} for each data point was averaged from over 10,000 repeated cycles. First, the baseline voltage-dependent switching probability was measured and fitted using Equation (1) (Fig. 1e). To characterize the thermal sensitivity, we measured the switching probability immediately after applying a pre-heating pulse (0.9 V, 50–500 ns) followed by a 20 ns RESET pulse to initialize the device in the parallel state (Fig. 1f). Subsequently, the thermal relaxation dynamics were characterized by introducing a variable cooling delay after a fixed pre-heating pulse (0.9 V, 500 ns) (Fig. 1g). The experimental data across all thermal states were fitted using Equation (1) by varying only the parameter x_0 while keeping other parameters constant, thereby establishing x_0 as the state variable representing the device temperature.

$$P_{sw} = \frac{L}{1 + e^{-k(x-x_0)}} \quad (1)$$

$$\Delta x_0 = aV_{input}^2 + bV_{input} \quad (2)$$

$$\Delta x_0 = A + B \cdot e^{-k \cdot t} \quad (3)$$

To quantify the voltage-dependent heating, the device was subjected to pre-heating pulses of varying amplitudes with a fixed duration (150 ns plateau, excluding 20 ns rise/fall times restricted by 4200A-SCS). The resulting state was immediately probed

using a 0.83 V, 150 ns pulse. The induced state shift, Δx_0 , was extracted and fitted as a function of the pre-pulse voltage using Equation (2). Similarly, cooling dynamics were quantified by heating the device to a high temperature using a train of five pre-heating pulses (comprising a 20 ns rise, 0.93 V/150 ns Set, 20 ns fall, -0.8 V/20 ns Reset, and 20 ns fall; total 230 ns per period), followed by variable cooling intervals (0–5000 ns). The decay of Δx_0 over time was fitted using Equation (3) (Fig. S1). The accuracy of the derived thermal model was validated by comparing the predicted state with experimental results from a sequence of three consecutive pulses (0.83 V, 150 ns each), showing good agreement (Fig. S3). This accuracy is further corroborated by the hardware-in-the-loop (HIL) experimental results presented in Section V (Fig. 5c). These hardware-extracted state evolution functions were utilized for all neural network experiments reported in this work.

MTJ-based neuron circuit design and area estimation

A basic MTJ-based stochastic neuron circuit is illustrated in Fig. 1d. To enhance temporal processing capabilities and robustness, we implemented a differential neuron architecture (Fig. S6). This design comprises two elementary neurons: a "temporal" neuron utilizing a thermally sensitive MTJ (e.g., 200 nm diameter) generating the output $Spike_t$, and a "reference" neuron utilizing a thermally insensitive MTJ (e.g., 100 nm diameter) (Fig. S7) generating $Spike_{ref}$. The two devices share the same switching probability at baseline state. The differential unit provides two output channels: $Spike_{ref}$, representing the instantaneous input intensity, and the difference signal $Spike_d = Spike_t - Spike_{ref}$, encoding historical thermal information. This operation is implemented using a subtractor circuit connecting the two neurons. To minimize the circuit footprint, the voltage-dividing resistors shown in Fig. 1d were replaced by MTJ devices of equivalent resistance, and the comparator was implemented using two series-connected CMOS inverters⁶⁴. In the system architecture, a single input feeds into N identical differential neurons. The outputs are average-pooled before transmission to the synapse, effectively performing N parallel Monte Carlo simulations within a single time step. All IPNet simulations, as well as power and area estimations reported in this study, are based on this differential neuron circuit configuration.

Given the negligible footprint of BEOL-integrated MTJs compared to the CMOS logic, the circuit area is determined by the transistor count. For the complete differential neuron comprising 24 transistors (6 inverters and 2 AND gates), the total area is estimated to be $\sim 1.5 \text{ um}^2$, based on a standard 28 nm technology node ($F = 28 \text{ nm}$) and a layout factor of $80 F^2$ per transistor.

Neural network training and evaluation

All neural network training and evaluation were implemented in a Python 3.10 environment with CUDA 12.8. Computations were performed using NVIDIA A800 or H100 GPUs.

***n*-back.** All networks (IPNet, LSTM, and LIF-SNN implemented via SpikingJelly⁶⁵) utilized a 225-225-2 topology. For the LSTM, the intermediate stage consisted of a single recurrent layer with 225 hidden units. Specifically, the IPNet and LIF-SNN incorporated neurons at the input layer, whereas the LSTM received inputs directly via synapses. The input images (225 pixels) consisted of a 3×3 grid of 5×5 pixel blocks, where a total of 8 distinct categories (each represents a letter from A to H) were encoded by randomly coloring 4 out of the 9 blocks. Data were input serially in sequences of 20 randomly sampled patterns. At each time step, the network determined if the current input matched the input presented *n* steps earlier. The performance was evaluated using the metric $PR = TPR - FPR$ ⁴³, excluding the first *n* steps of each sequence.

Free recall. The networks (IPNet and LSTM) utilized a fully connected architecture with a 225 - 512 - 50 topology. The LSTM consisted of a single recurrent layer with 512 hidden units. As in the N-back task, the IPNet incorporated neurons at the input layer, whereas the LSTM received inputs directly via synapses. The input images were encoded using the same block-based method as described above, but with a total of 50 distinct categories. For each trial, a sequence of 15 unique patterns sampled from the 50 categories was input serially. Following the presentation of the sequence and a variable delay period of *T* time steps, the network was required to output the class indices of all 15 presented items simultaneously. In this free recall task, the network was only required to identify the presence of the items, independent of their temporal order. The recall accuracy was quantified as a function of the item's serial position during input and the duration of the delay period *T*.

Proactive and retroactive interference. The networks were configured with a 900-225-50 topology. Consistent with the previous tasks, the IPNet incorporated neurons at the input layer, whereas the LSTM comprised a single recurrent layer with 225 hidden units. To investigate the role of data similarity, inputs were generated using two distinct encoding schemes: one-hot encoding (representing orthogonal, non-overlapping inputs) and 4-out-of-9 coding (representing inputs with partial similarity). For both schemes, the input dimension was standardized to 900 units, representing 50 distinct categories. The experiment consisted of three conditions, each spanning 3 time-steps. In the control (no-interference) task, the target memory item was presented at the second time-step ($t=2$), with null inputs at $t=1$ and $t=3$. The network was trained to output the label of the target item at the end of the sequence. In the proactive interference task, a distractor item was presented at $t=1$, preceding the target item at $t=2$. In the retroactive

interference task, the distractor was presented at $t=3$, following the target item at $t=2$. In all interference trials, the distractor and target were drawn from the same distribution. To emulate the protocol of analogous human cognitive tasks, the networks were trained to retain both the distractor and the target; however, the interference effect was characterized specifically by the recall accuracy of the target item.

Dynamic vision tasks. To enhance the processing capability for complex visual stimuli, convolutional neural network (CNN)-based architectures were adopted as the backbone for both the proposed IPNet and the baseline models. For the IPNet architectures, we utilized fully spiking SEW-ResNet frameworks⁶⁶, where IPNet18, IPNet34, and IPNet50 were adapted from SEW-ResNet18, SEW-ResNet34, and SEW-ResNet50, respectively. All IPNet models (including FCN-IPNet in memory tasks) were trained directly using the Backpropagation Through Time (BPTT) algorithm. Unless otherwise specified, the input layer was replaced by the proposed differential neuron block (designated as the IPLayer). In contrast, all subsequent layers employed the thermally insensitive stochastic MTJ neuron model; these neurons are implemented without the differential architecture, strictly simulating the standard circuit configuration illustrated in Fig. 1d. Additionally, the original Batch Normalization (BatchNorm) layers in the SEW-ResNet were replaced with Root Mean Square Normalization (RMSNorm). Specific to the Time-Reversed DVS Gesture task, the IPLayer was configured to perform 8 parallel Monte Carlo simulations (via average pooling of 8 identical neurons per time step), whereas all downstream MTJ neurons operated with a single simulation count, a configuration found to yield optimal performance. For the baselines, the ResNet18-LSTM model integrated the standard PyTorch ResNet18 backbone with a single-layer LSTM containing 1024 hidden units, positioned between the backbone output and the final classification layer. The (2+1)D ResNet18 baseline utilized the standard implementation provided in the PyTorch library. To accommodate varying input spatial dimensions across different tasks, the first convolutional layer of all models was modified accordingly. To ensure a fair comparison, all models underwent equivalent hyperparameter optimization.

Experimental settings for hardware-in-the-loop (HIL)

Network architecture and hardware mapping. To facilitate physical implementation, a customized IPNet architecture was developed. The convolutional backbone remains identical to the IPNet18; however, the thermally sensitive IPLayer was relocated from the input stage to the post-convolution stage. Specifically, the feature maps from the convolutional backbone are projected via a fully connected (FC) layer to an IPLayer comprising 49 neurons, which is then connected to the final output classification layer via another FC layer. To map these 49 logical neurons into limited hardware resources,

we employed a time-division multiplexing strategy: 7 physical thermally sensitive MTJ devices were each reused 7 times. A single thermally insensitive MTJ served as the shared reference device for the differential neuron architecture. During both training and inference, the network processes a sequence of 4 consecutive video frames serially for each steering angle prediction, ensuring that the thermal history within the MTJs is effectively utilized for temporal processing. For comparison, the ResNet18-LSTM baseline was adapted with a similar topology, where the LSTM hidden size was reduced from 1024 to 49 units to match the scale of the hardware IPNet.

HIL execution protocol. First, the network was trained entirely in a Python software environment to obtain optimal synaptic weights. Subsequently, inference was performed on the test dataset, which comprised two distinct 600-frame video segments totaling 1,200 samples (results visualized in Fig. 5e and Fig. S8), to extract the precise voltage inputs destined for the IPLayer at each time step. These voltage values were encoded into pulse sequences and applied to the corresponding physical MTJ devices (both the sensitive and reference units) via radio-frequency (RF) probes, preserving the exact temporal order of the input frames. Crucially, identical input sequences were applied to both the thermally sensitive and reference MTJs. This setup aligned with the software training protocol, where the reference neuron was explicitly modeled to exhibit a switching probability independent of historical pulses, thereby experimentally validating that the fabricated devices can support both memory-dependent and memory-independent modes under identical stimulation. The switching state (Parallel/Anti-Parallel) of the MTJs was measured to determine the spiking output. To emulate the average pooling mechanism used in the software model, 32 repeated Monte Carlo simulations were conducted for each neuron per frame on the hardware. Finally, the experimentally obtained average firing rates were fed back into the software environment to compute the final steering angle through the last fully connected layer.

Memory energy measurement

IPNet energy estimation. The energy for memory processing of the IPNet was derived from direct current-voltage (I - V) characterizations of the MTJ devices of IPLayer. For a representative thermally sensitive MTJ (ID: R09C11), the resistance states were measured as $R_P = 230\Omega$ and $R_{AP} = 410\Omega$. Under a standard operating voltage of 0.80 V (yielding a baseline switching probability of $\approx 19.72\%$) and a total pulse protocol duration of 230 ns (encompassing both Set and Reset phases), the energy consumption per cycle is approximately 450 pJ. The thermally insensitive reference MTJ, designed with higher resistance, consumes approximately 82 pJ per cycle under identical conditions. The power dissipation of the auxiliary CMOS circuitry (24 transistors) in the differential neuron is negligible compared to the MTJ write energy. Consequently,

the total energy consumption for a single differential neuron operation is estimated at ≈ 0.6 nJ. To project the system-level energy for the DVS Gesture task ($2 \times 128 \times 128$ resolution, 50 frames per sample), we considered an average input spike density of 8.9%. This yields an estimated memory energy consumption of 87 μ J ($2 \times 128 \times 128 \times 8.9\% \times 50 \times 0.6$ nJ) per sample for the IPNet. While optimal performance in general tasks may require 4-16 parallel Monte Carlo simulations (increasing consumption to 348-1392 μ J), it is notable that for the specific Time-Reversed DVS Gesture task, a single simulation count is sufficient to outperform the ResNet-LSTM baseline, maintaining the minimal energy footprint.

Baseline model energy measurement. To quantify the specific energy cost attributed to memory processing in conventional ANN memory architectures, we measured the incremental power consumption relative to a static backbone. Experiments were conducted on an NVIDIA A800 GPU (fabricated on an advanced TSMC process node). During inference, power consumption was monitored using `pynvml`⁶⁷ (NVIDIA’s own energy reporting framework). We compared the inference energy of the temporal models (ResNet18-RNN, ResNet18-LSTM, and (2+1)D ResNet18) against a standard static ResNet18 baseline, with all models utilizing identical batch sizes and hyperparameters. Energy values represent the median over 20 iterations of the Time-Reversed DVS Gesture test set. The incremental energy costs per sample, attributed to the memory/temporal components, were measured as 0.21 J for the RNN, 0.25 J for the LSTM, and 7.91 J for the (2+1)D ResNet18. Comparative results indicate that the proposed IPNet architecture reduces memory-specific energy consumption by 300-3,000 times of magnitude relative to standard recurrent baselines (RNN/LSTM), extending to approximately 10,000-100,000 times orders of magnitude when compared against computationally intensive spatiotemporal models such as the (2+1)D ResNet.

References

1. Constantinidis, C. & Klingberg, T. The neuroscience of working memory capacity and training. *Nat. Rev. Neurosci.* **17**, 438–449 (2016).
2. Baddeley, A. Working memory. in *Memory* (Routledge, 2020).
3. Luck, S. J. & Vogel, E. K. The capacity of visual working memory for features and conjunctions. (1997).
4. Sahakian, A., Gayet, S., Paffen, C. L. E. & Van der Stigchel, S. The rise and fall of memories: Temporal dynamics of visual working memory. *Mem. Cognit.* **53**, 2406–2423 (2025).
5. Olivers, C. N. L., Peters, J., Houtkamp, R. & Roelfsema, P. R. Different states in visual working memory: when it guides attention and when it does not. *Trends Cogn. Sci.* **15**, 327–334 (2011).
6. Brady, T. F., Robinson, M. M. & Williams, J. R. Noisy and hierarchical visual memory across timescales. *Nat. Rev. Psychol.* **3**, 147–163 (2024).
7. Hassabis, D., Kumaran, D., Summerfield, C. & Botvinick, M. Neuroscience-Inspired Artificial Intelligence. *Neuron* **95**, 245–258 (2017).
8. Collins, J., Sohl-Dickstein, J. & Sussillo, D. Capacity and Trainability in Recurrent Neural Networks. Preprint at <https://doi.org/10.48550/arXiv.1611.09913> (2017).
9. Nazeri, A. & Pisu, P. LSTM-based Load Forecasting Robustness Against Noise Injection Attack in Microgrid. Preprint at <https://doi.org/10.48550/arXiv.2304.13104> (2023).

10. Prater, R., Hanne, T. & Dornberger, R. Generalized Performance of LSTM in Time-Series Forecasting. *Appl. Artif. Intell.* **38**, 2377510 (2024).
11. de Haan, P., Jayaraman, D. & Levine, S. Causal Confusion in Imitation Learning. in *Advances in Neural Information Processing Systems* vol. 32 (Curran Associates, Inc., 2019).
12. Chitta, K. *et al.* TransFuser: Imitation With Transformer-Based Sensor Fusion for Autonomous Driving.
13. Hu, Y. *et al.* Planning-oriented Autonomous Driving. in *2023 IEEE/CVF Conference on Computer Vision and Pattern Recognition (CVPR)* 17853–17862 (IEEE, Vancouver, BC, Canada, 2023). doi:10.1109/CVPR52729.2023.01712.
14. Patterson, D. *et al.* Carbon Emissions and Large Neural Network Training.
15. Khan, S. *et al.* Transformers in Vision: A Survey. *ACM Comput Surv* **54**, 200:1-200:41 (2022).
16. Tavanaei, A., Ghodrati, M., Kheradpisheh, S. R., Masquelier, T. & Maida, A. Deep learning in spiking neural networks. *Neural Netw.* **111**, 47–63 (2019).
17. Delbruck, T. Frame-free dynamic digital vision. (2008).
18. Liao, F., Zhou, F. & Chai, Y. Neuromorphic vision sensors: Principle, progress and perspectives. *J. Semicond.* **42**, 013105 (2021).
19. Bellec, G., Salaj, D., Subramoney, A., Legenstein, R. & Maass, W. Long short-term memory and Learning-to-learn in networks of spiking neurons.
20. Yao M. *et al.* Spike-driven Transformer. *Adv. Neural Inf. Process. Syst.* **36**, 64043–64058 (2023).

21. Roy, K., Jaiswal, A. & Panda, P. Towards spike-based machine intelligence with neuromorphic computing. *Nature* **575**, 607–617 (2019).
22. Indiveri, G. Neuromorphic is dead. Long live neuromorphic. *Neuron* **113**, 3311–3314 (2025).
23. Eshraghian, J. K. *et al.* Training Spiking Neural Networks Using Lessons From Deep Learning. *Proc. IEEE* **111**, 1016–1054 (2023).
24. Rueckauer, B., Lungu, I.-A., Hu, Y., Pfeiffer, M. & Liu, S.-C. Conversion of Continuous-Valued Deep Networks to Efficient Event-Driven Networks for Image Classification. *Front. Neurosci.* **11**, (2017).
25. Li, G. *et al.* Brain-Inspired Computing: A Systematic Survey and Future Trends. *Proc. IEEE* **112**, 544–584 (2024).
26. Christensen, D. V. *et al.* 2022 roadmap on neuromorphic computing and engineering. *Neuromorphic Comput. Eng.* **2**, 022501 (2022).
27. Marković, D., Mizrahi, A., Querlioz, D. & Grollier, J. Physics for neuromorphic computing. *Nat. Rev. Phys.* **2**, 499–510 (2020).
28. Ielmini, D. & Wong, H.-S. P. In-memory computing with resistive switching devices. *Nat. Electron.* **1**, 333–343 (2018).
29. Khan, A. I., Keshavarzi, A. & Datta, S. The future of ferroelectric field-effect transistor technology. *Nat. Electron.* **3**, 588–597 (2020).
30. Le Gallo, M. & Sebastian, A. An overview of phase-change memory device physics. *J. Phys. Appl. Phys.* **53**, 213002 (2020).
31. Roy, K. *et al.* Spintronic neural systems. *Nat. Rev. Electr. Eng.* **1**, 714–729 (2024).

32. Sangwan, V. K. & Hersam, M. C. Neuromorphic nanoelectronic materials. *Nat. Nanotechnol.* **15**, 517–528 (2020).
33. Rathi, N. *et al.* Exploring Neuromorphic Computing Based on Spiking Neural Networks: Algorithms to Hardware. *ACM Comput Surv* **55**, 243:1-243:49 (2023).
34. Shaban, A., Bezugam, S. S. & Suri, M. An adaptive threshold neuron for recurrent spiking neural networks with nanodevice hardware implementation. *Nat. Commun.* **12**, 4234 (2021).
35. Yuan, R. *et al.* A neuromorphic physiological signal processing system based on VO₂ memristor for next-generation human-machine interface. *Nat. Commun.* **14**, 3695 (2023).
36. Egorov, A. V., Hamam, B. N., Fransén, E., Hasselmo, M. E. & Alonso, A. A. Graded persistent activity in entorhinal cortex neurons. *Nature* **420**, 173–178 (2002).
37. Fitz, H. *et al.* Neuronal spike-rate adaptation supports working memory in language processing. *Proc. Natl. Acad. Sci.* **117**, 20881–20889 (2020).
38. Amir, A. *et al.* A Low Power, Fully Event-Based Gesture Recognition System. in *2017 IEEE Conference on Computer Vision and Pattern Recognition (CVPR)* 7388–7397 (IEEE, Honolulu, HI, 2017). doi:10.1109/CVPR.2017.781.
39. Donahue, J. *et al.* Long-Term Recurrent Convolutional Networks for Visual Recognition and Description. in 2625–2634 (2015).
40. Qiu, X., Yan, F. & Liu, H. A difference attention ResNet-LSTM network for epileptic seizure detection using EEG signal. *Biomed. Signal Process. Control* **83**,

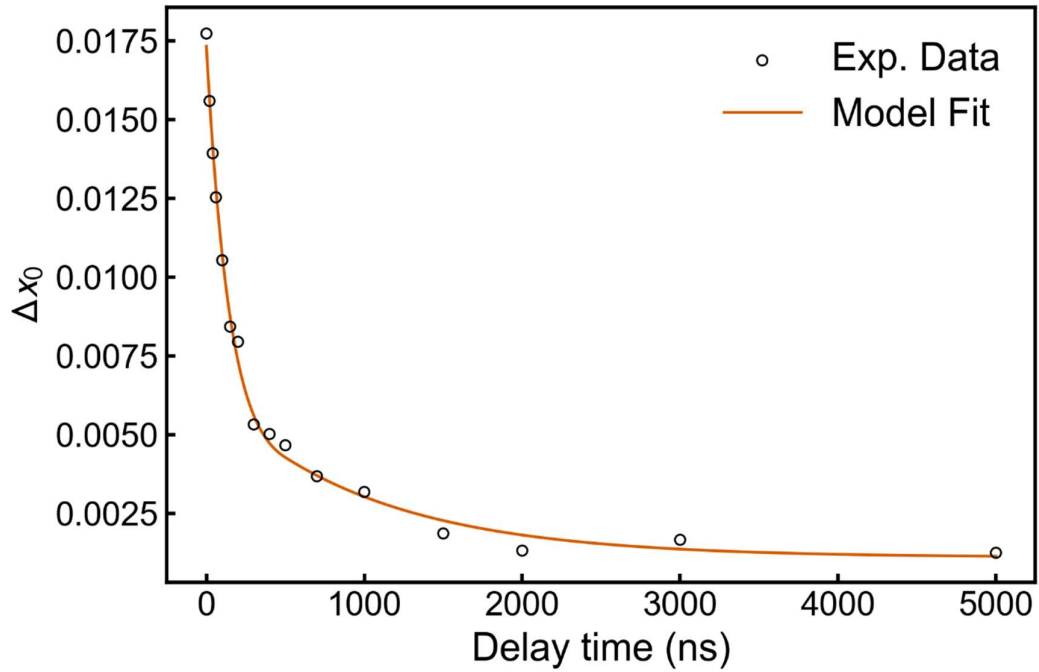
104652 (2023).

41. Tran, D. *et al.* A Closer Look at Spatiotemporal Convolutions for Action Recognition. in 6450–6459 (2018).
42. Kurenkov, A. *et al.* Artificial Neuron and Synapse Realized in an Antiferromagnet/Ferromagnet Heterostructure Using Dynamics of Spin–Orbit Torque Switching. *Adv. Mater.* **31**, 1900636 (2019).
43. Jaeggi, S. M., Buschkuhl, M., Perrig, W. J. & Meier, B. The concurrent validity of the *N*-back task as a working memory measure. *Memory* **18**, 394–412 (2010).
44. Lamichhane, B., Westbrook, A., Cole, M. W. & Braver, T. S. Exploring brain-behavior relationships in the N-back task. *NeuroImage* **212**, 116683 (2020).
45. Sakai, K., Rowe, J. B. & Passingham, R. E. Active maintenance in prefrontal area 46 creates distractor-resistant memory. *Nat. Neurosci.* **5**, 479–484 (2002).
46. Chatham, C. H. & Badre, D. Multiple gates on working memory. *Curr. Opin. Behav. Sci.* **1**, 23–31 (2015).
47. Jonides, J. & Nee, D. E. Brain mechanisms of proactive interference in working memory. *Neuroscience* **139**, 181–193 (2006).
48. Miller, E. K., Erickson, C. A. & Desimone, R. Neural Mechanisms of Visual Working Memory in Prefrontal Cortex of the Macaque. *J. Neurosci.* **16**, 5154–5167 (1996).
49. Glanzer, M. Two Storage Mechanisms in Free Recall I.
50. Schurgin, M. W. Visual memory, the long and the short of it: A review of visual working memory and long-term memory. *Atten. Percept. Psychophys.* **80**, 1035–

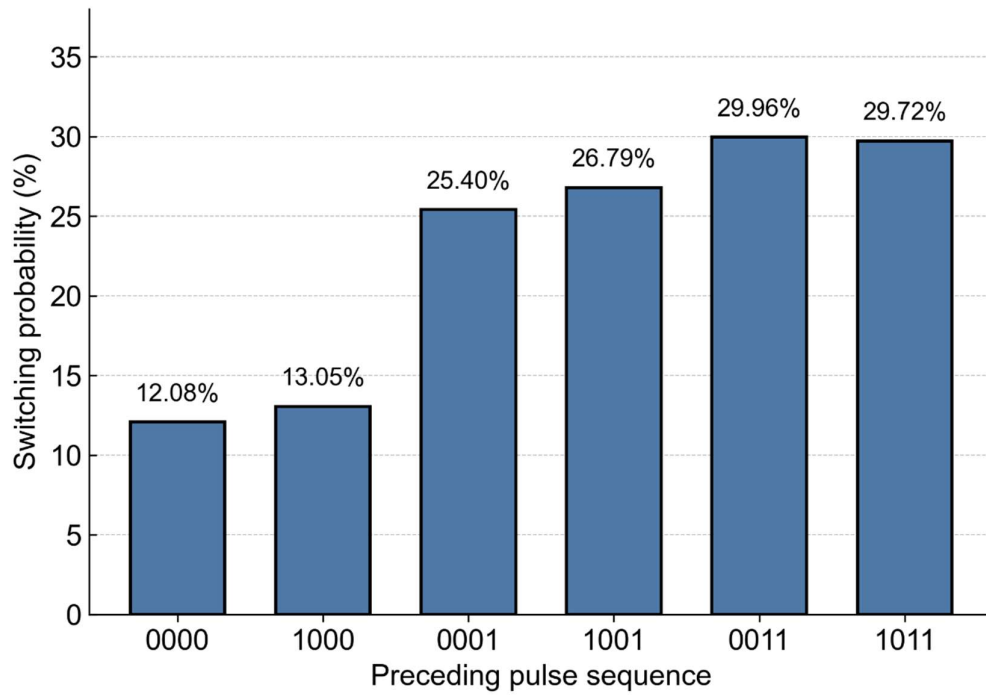
- 1056 (2018).
51. He, K., Zhang, X., Ren, S. & Sun, J. Deep Residual Learning for Image Recognition. in 770–778 (2016).
 52. Hu, Y., Binas, J., Neil, D., Liu, S.-C. & Delbruck, T. DDD20 End-to-End Event Camera Driving Dataset: Fusing Frames and Events with Deep Learning for Improved Steering Prediction. in *2020 IEEE 23rd International Conference on Intelligent Transportation Systems (ITSC)* 1–6 (IEEE, Rhodes, Greece, 2020). doi:10.1109/ITSC45102.2020.9294515.
 53. Maqueda, A. I., Loquercio, A., Gallego, G., Garcia, N. & Scaramuzza, D. Event-Based Vision Meets Deep Learning on Steering Prediction for Self-Driving Cars. in *2018 IEEE/CVF Conference on Computer Vision and Pattern Recognition* 5419–5427 (IEEE, Salt Lake City, UT, 2018). doi:10.1109/CVPR.2018.00568.
 54. Madjid, N. A. *et al.* Trajectory Prediction for Autonomous Driving: Progress, Limitations, and Future Directions. *Inf. Fusion* **126**, 103588 (2026).
 55. Bojarski, M. *et al.* End to End Learning for Self-Driving Cars. Preprint at <https://doi.org/10.48550/arXiv.1604.07316> (2016).
 56. Wen, C., Lin, J., Darrell, T., Jayaraman, D. & Gao, Y. Fighting Copycat Agents in Behavioral Cloning from Observation Histories. in *Advances in Neural Information Processing Systems* vol. 33 2564–2575 (Curran Associates, Inc., 2020).
 57. Land, M. F. & Lee, D. N. Where we look when we steer. *Nature* **369**, 742–744 (1994).

58. DeepSeek-R1 incentivizes reasoning in LLMs through reinforcement learning | Nature. <https://www.nature.com/articles/s41586-025-09422-z>.
59. Naveed, H. *et al.* A Comprehensive Overview of Large Language Models. *ACM Trans Intell Syst Technol* **16**, 106:1-106:72 (2025).
60. Lundqvist, M., Herman, P. & Miller, E. K. Working Memory: Delay Activity, Yes! Persistent Activity? Maybe Not. *J. Neurosci.* **38**, 7013–7019 (2018).
61. Panichello, M. F. *et al.* Intermittent rate coding and cue-specific ensembles support working memory. *Nature* **636**, 422–429 (2024).
62. Stokes, M. G. ‘Activity-silent’ working memory in prefrontal cortex: a dynamic coding framework. *Trends Cogn. Sci.* **19**, 394–405 (2015).
63. Zhou, F. & Chai, Y. Near-sensor and in-sensor computing. *Nat. Electron.* **3**, 664–671 (2020).
64. Liu, H. & Ohsawa, T. A binarized spiking neural network based on auto-reset LIF neurons and large signal synapses using STT-MTJs. *Jpn. J. Appl. Phys.* **62**, 044501 (2023).
65. Fang, W. *et al.* SpikingJelly: An open-source machine learning infrastructure platform for spike-based intelligence. *Sci. Adv.* **9**, eadi1480 (2023).
66. Fang, W. *et al.* Deep Residual Learning in Spiking Neural Networks. in *Advances in Neural Information Processing Systems* vol. 34 21056–21069 (Curran Associates, Inc., 2021).
67. NVIDIA Management Library (NVML). *NVIDIA Developer* <https://developer.nvidia.com/management-library-nvml>.

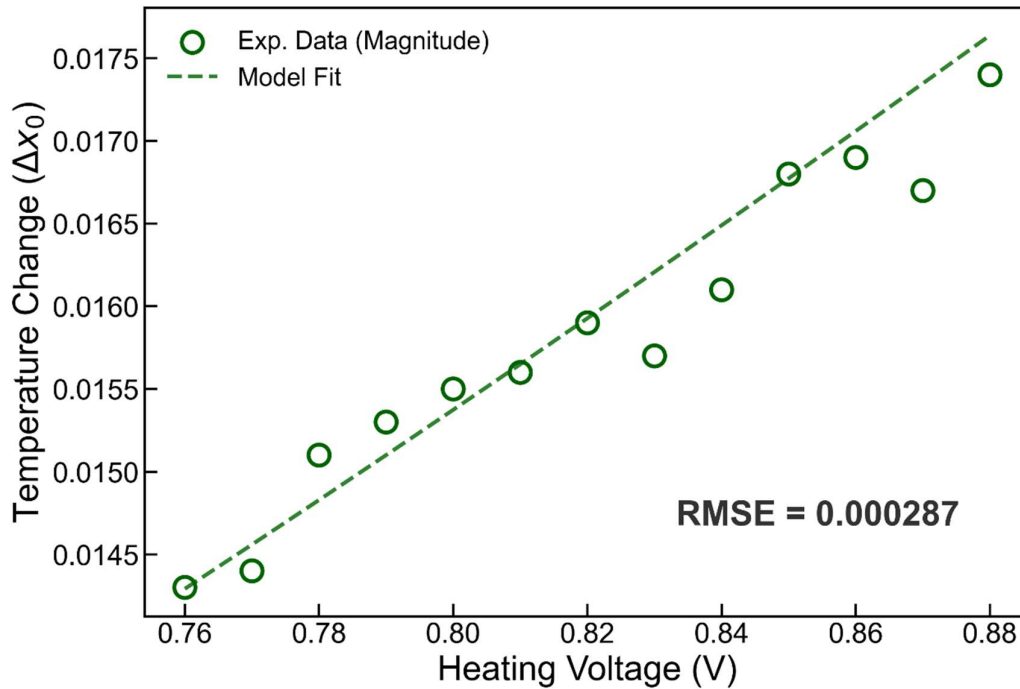
Supplementary Information



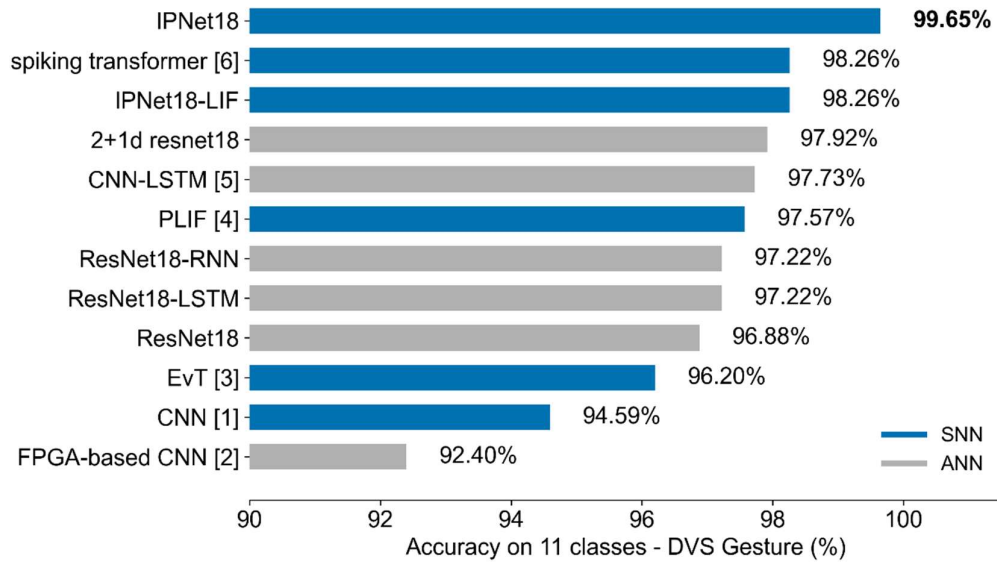
Supplementary Fig. 1. Temporal decay of the sigmoid mean parameter x_0 . The data show the relaxation of x_0 following a train of five voltage pulses (0.9 V amplitude). The solid orange line represents the best fit using a two-segment piecewise exponential model with a breakpoint at 500 ns.



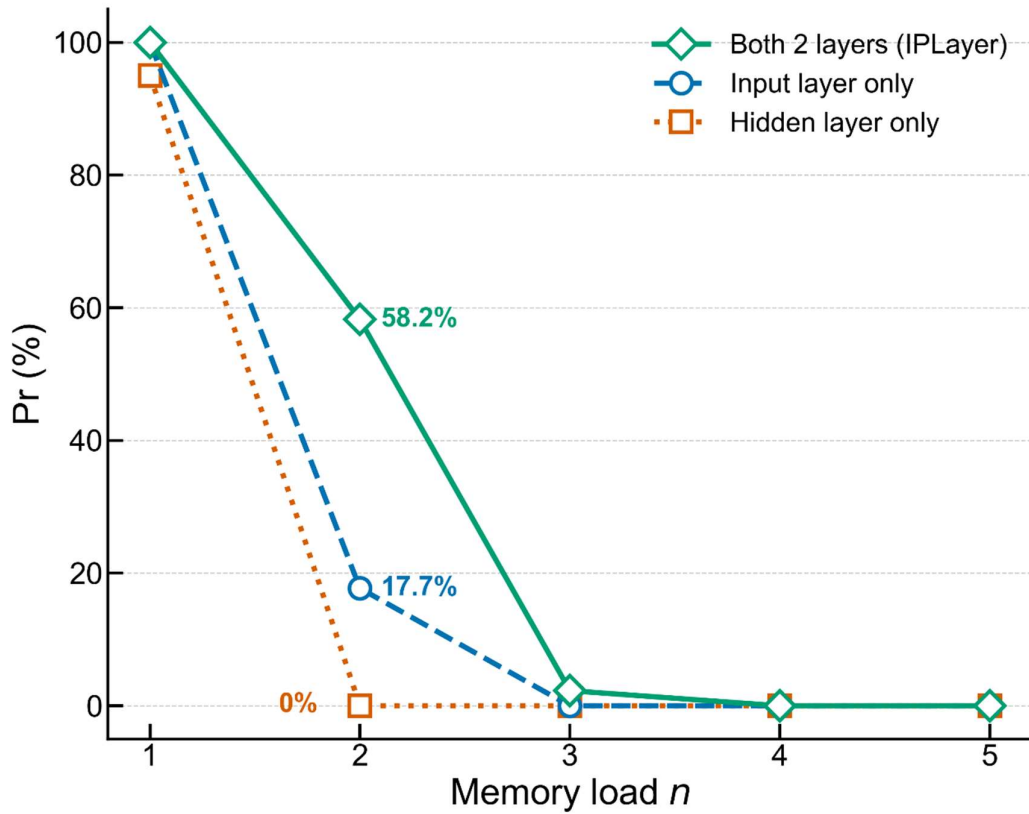
Supplementary Fig. 2. Dependence of MTJ switching probability on the preceding pulse sequence. The input consists of a four-step sequence where '1' and '0' denote the presence and absence of an input spike (0.85 V, 230 ns period), respectively. Switching probability was assessed using a probe pulse (0.83 V, 150 ns) applied immediately after the sequence. The digits follow chronological order. For instance, '1000' indicates a pulse at the first time step followed by three idle steps.



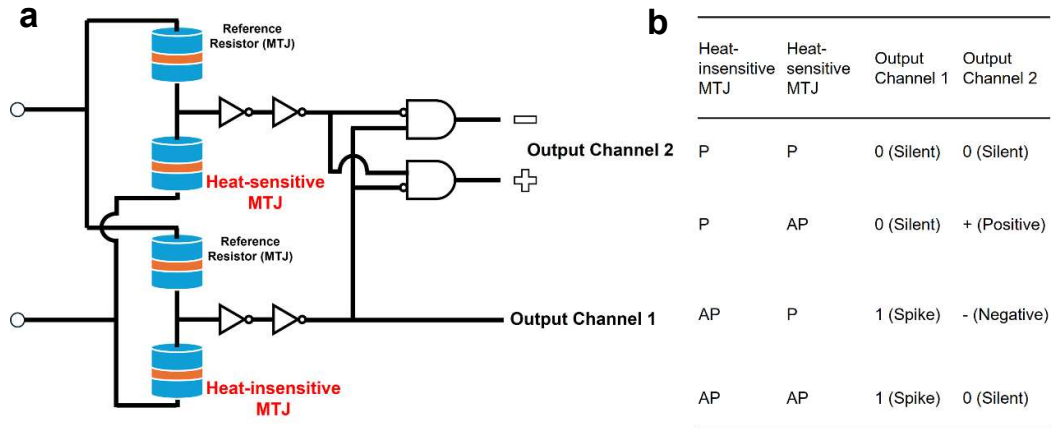
Supplementary Fig. 3. Validation of the thermal intrinsic plasticity algorithmic model. The plot compares the modeled (dashed line) and experimentally measured (open circles) temperature change (Δx_0) of the MTJ following three pre-pulses (230 ns period) at varying voltages. The Δx_0 values were derived from the switching probability measured using a probe pulse (0.83 V, 150 ns) (see **Methods**). The algorithmic simulation agrees well with the experimental data, with a root-mean-square error (RMSE) of 0.000287.



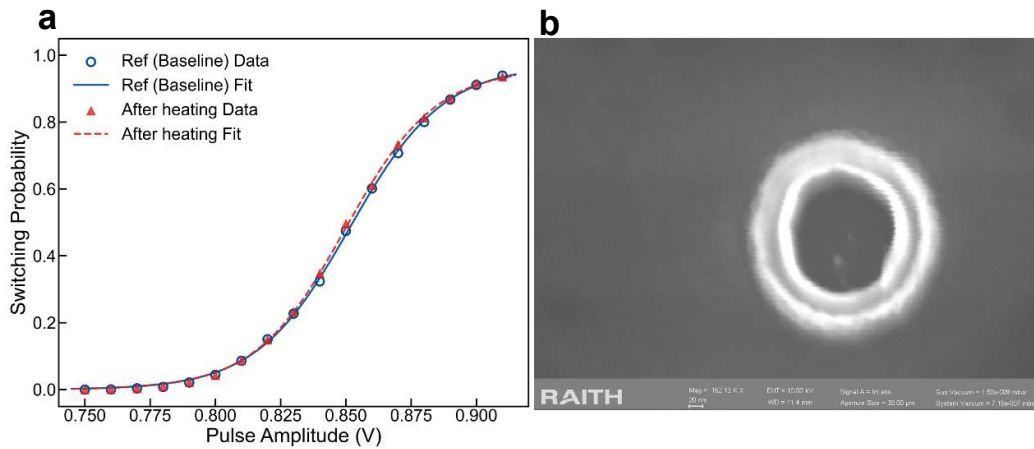
Supplementary Fig. 4. Validation of the thermal intrinsic plasticity algorithmic model. The bar chart compares the classification accuracy of IPNet18 with other reported models¹⁻⁶ on the 11-class DVS Gesture task. Blue and gray bars denote models based on Spiking Neural Networks (SNNs) and Artificial Neural Networks (ANNs), respectively.



Supplementary Fig. 5. Performance of the FCN-based IPNet on the n -back task with varying IPLayer placements. The model is built on a fully connected network (FCN) topology with 225 input, 225 hidden, and 2 output neurons. Performance rate (P_r (%)) is plotted as a function of memory load n . The green solid line with diamonds denotes the configuration where standard neurons in both the input and hidden layers are replaced by IPNeurons ("Both 2 layers"). The blue dashed line with circles and the orange dotted line with squares represent models with IPNeurons implemented only in the input layer ("Input layer only") or the hidden layer ("Hidden layer only"), respectively. Annotated percentages indicate the P_r at $n=2$.

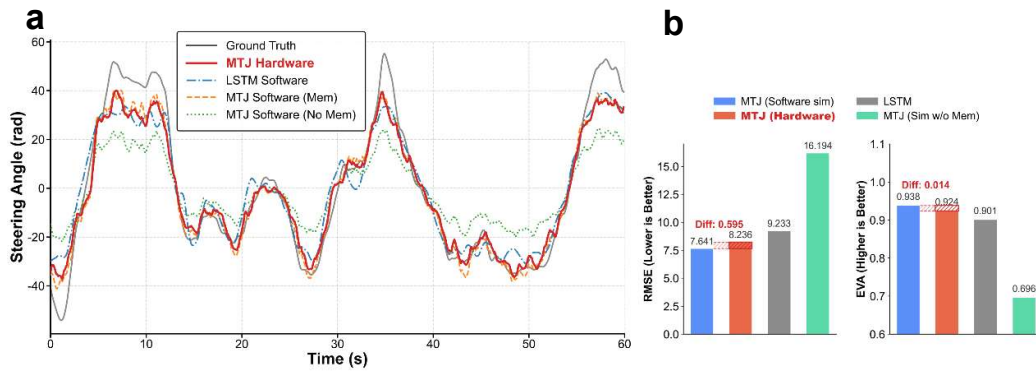


Supplementary Fig. 6. Schematic of the MTJ-based differential intrinsic plasticity neuron circuit. **a**, Schematic of the circuit comprising two active MTJs (text in red), two reference MTJs, and peripheral CMOS. The active MTJs differ in thermal sensitivity (heat-sensitive vs. heat-insensitive). **b**, Truth table summarizing the output logic. Output Channel 1 depends solely on the heat-insensitive MTJ state (firing in the antiparallel/AP state; silent in the parallel/P state). Output Channel 2 generates ternary outputs (Positive/Negative/Zero) based on the combined resistance states of both active MTJs. In this digital implementation, two physical output lines are used to represent positive and negative spikes, respectively.



Supplementary Fig. 7. Characterization of thermal sensitivity in a 100 nm MTJ.

a, Switching probability as a function of pulse amplitude. Blue circles represent baseline data collected without pre-pulses, while red triangles denote measurements taken immediately after three pulses (0.9 V SET, 230 ns total cycle). The solid and dashed lines indicate the corresponding sigmoid fits. The overlapping curves demonstrate that the switching probability of the 100 nm MTJ is insensitive to the heating protocol, in sharp contrast to the behavior of the 200 nm MTJ shown in Fig. 1f, 1g. **b**, Top-view scanning electron microscopy (SEM) image of a 100 nm MTJ.



Supplementary Fig. 8. Additional hardware-in-the-loop evaluation on a distinct driving segment. **a**, Steering angle trajectories over an additional 600-frame test sequence (separate from the segment in Fig. 5). **b**, Quantitative metrics (RMSE and EVA) for this 600 frames segment.

Supplementary References

1. Amir, A. *et al.* A Low Power, Fully Event-Based Gesture Recognition System. in 7243–7252 (2017).
2. Fu, Z. & Ye, W. A 593nJ/Inference DVS Hand Gesture Recognition Processor Embedded With Reconfigurable Multiple Constant Multiplication Technique. *IEEE Transactions on Circuits and Systems I: Regular Papers* **71**, 2749–2759 (2024).
3. Sabater, A., Montesano, L. & Murillo, A. C. Event Transformer. A Sparse-Aware Solution for Efficient Event Data Processing. in 2677–2686 (2022).
4. Fang, W. *et al.* Incorporating Learnable Membrane Time Constant To Enhance Learning of Spiking Neural Networks. in 2661–2671 (2021).
5. Innocenti, S. U., Becattini, F., Pernici, F. & Del Bimbo, A. Temporal Binary Representation for Event-Based Action Recognition. in *2020 25th International Conference on Pattern Recognition (ICPR)* 10426–10432 (2021).
doi:10.1109/ICPR48806.2021.9412991.
6. Lin, X., Liu, M. & Chen, H. Spike-HAR++: an energy-efficient and lightweight parallel spiking transformer for event-based human action recognition. *Front. Comput. Neurosci.* **18**, (2024).